Article

Microstructural and Magnetic Properties of Polyamide-Based Recycled Composite with Iron Oxide Nanoparticles

Lucas G. Dos Santos , Daina D. A. Buelvas * , Daniel F. Valezi , Bruno L. S. Vicentin ,
Christian Manuel Moreno Rocha , Eduardo Di Mauro , Felipe de A. La Porta *

Posted Date: 14 November 2024

doi: 10.20944/preprints202411.1029.v1

Keywords: Recycled Polyamide composite; Magnetite; Maghemite; Environmental; Nanocomposites

Article

Microstructural and Magnetic Properties of Polyamide-Based Recycled Composite with Iron Oxide Nanoparticles

Lucas G. Dos Santos [1], Daina D. A. Buelvas [2,*], Daniel F. Valezi [1], Bruno L. S. Vicentin [3], Christian M. M. Rocha [4,5], Eduardo Di Mauro [1] and Felipe de A. La Porta [2,6,*]

[1] Department of Physics, State University of Londrina, Londrina, Paraná- Rodovia Celso Garcia Cid, PR-445, Km 380, Londrina 86057-970, Brazil
[2] Nanotechnology and Computational Chemistry Laboratory, Federal University of Technology—Paraná, Paraná- Av. dos Pioneiros, 3131 - Jardim Morumbi, Londrina 86036-370, Brazil
[3] Academic Department of Physics, Federal University of Technology—Paraná, Paraná-Rua Doutor Washington Subtil Chueire, 330, Ponta Grossa 84017-220, Brazil
[4] Department of Energy, Universidad de la Costa CUC, Barranquilla, Colombia, calle 58#55-66, 080003
[5] Department of Electronics and Computing, University of Santiago de Compostela, Rúa Lope Gómez de Marzoa, s/n 15782, Spain
[6] Post-Graduation Program in Chemistry, State University of Londrina, Londrina, Paraná- Rodovia Celso Garcia Cid, PR-445, Km 380, Londrina 86057-970, Brazil
* Correspondence: dainabuelvas@gmail.com (D.D.A.B.); felipelaporta@utfpr.edu.br (F.d.A.L.P.)

Abstract: This study explores a sustainable approach to developing magnetic nanocomposites by synthesizing a mixed-phase iron oxide (IO) and recycled polyamide (RPA) composite derived from textile waste. The RPA/IO nanocomposite's microstructural and magnetic properties were characterized using X-ray diffraction (XRD) with Rietveld refinement, scanning, and transmission electron microscopy (SEM, TEM), vibrating sample magnetometry (VSM), and Mössbauer spectroscopy. XRD confirmed the presence of both magnetite (Fe_3O_4) and maghemite (γ-Fe_2O_3) phases, with Rietveld refinement indicating 79.4 wt% Fe_3O_4. SEM and TEM showed a porous, agglomerated IO surface morphology with an average particle size of 14 nm. Magnetic analysis revealed ferrimagnetic and superparamagnetic behavior, with VSM showing saturation magnetization values of 22.2 emu/g at 5 K and 19.1 emu/g at 300 K. Anisotropy constants were estimated at 2.90×10^5 and 1.26×10^5, respectively, for IO and the composite, with a blocking temperature of approximately 149 K. Mössbauer spectroscopy confirmed both Fe_3O_4 and γ-Fe_2O_3 phases, and the RPA matrix did not significantly impact the IO's crystal structure. These findings contribute to understanding the magnetic behavior of IO and their nanocomposites, which is crucial for their potential applications in emerging technologies.

Keywords: recycled polyamide composite; magnetite; maghemite; environmental; nanocomposites

1. Introduction

The textile and clothing industry's reliance on polyamides (PAs), or Nylons, creates a significant environmental challenge due to the large volumes of solid waste generated annually [1,2]. While these synthetic fibers offer high elasticity, durability, and resistance to various environmental factors, their non-biodegradable nature results in long-term pollution as a significant portion ends up in landfills [3–7].

Although ongoing efforts to reduce and recycle PAs (RPAs) face obstacles, the urgency for sustainable solutions in the textile industry is undeniable. PAs are versatile, semi-crystalline thermoplastics derived from petroleum [8,9], possess excellent mechanical and chemical properties, making them indispensable across various industries [10–13].

However, the RPAs, particularly from post-consumer textile waste, is complex due to contamination and degradation during processing [3,4]. This underscores the importance of developing advanced recycling methods and incorporating RPAs into high-performance materials, which in turn can transform the textile industry, reducing its environmental burden and ensuring a more sustainable future.

RPAs, despite their potential for sustainability, often falls short in performance compared to virgin materials [14]. To address these limitations, various fillers (organic and inorganic) are commonly incorporated into PA to create composites, leading to improving their properties and reducing costs. Recently, PAs nanocomposites based on a wide range of nanometer-scale fillers, such as clay particles [15], titanium [16], cellulose nanofibers [17], graphene [18], and iron oxide (IO) [19,20], have widely been studied. Among these nanomaterials, IO polymorphs stand out as highly promising candidate for various emerging technologies, owing to their abundance, cost-effectiveness, and diverse functionalities [21]. Particularly, Fe_3O_4 (also known as magnetite) is a significant iron oxide with mixed-valence IO structure, contains both Fe^{2+} and Fe^{3+} ions within its crystal lattice, giving its characteristic ferrimagnetic properties, distinguishing it from the solely Fe^{3+}-containing polymorphs [22]. The magnetite phase has an inverse cubic spinel structure ($a = 8.396$ Å) with Fe^{3+} ions distributed in both tetrahedral and octahedral sites, and Fe^{2+} ions exclusively in octahedral sites [23]. Under certain conditions, Fe^{2+} ions within magnetite are susceptible to oxidation, a process that can result in the transformation to the maghemite (γ-Fe_2O_3), another IO polymorph with only contains Fe^{3+} ions [24–26]. Both magnetite and maghemite been extensively studied for their valuable magnetic properties [27–31].

The combination of IO nanoparticles with polymeric matrices leads to functional materials with enhanced magnetic, mechanical, thermal, and even biological properties [19,32–35]. One key advantage is their ability to form a well-distributed network within the polymer matrix, facilitating nanoscale interactions that directly influence the overall properties of the material [36,37]. This maximizes the contact between the IO nanoparticles and the RPA matrix, improving functionality and consistency. The versatility and economic benefits of IO nanoparticles make them an attractive option for enhancing the performance of RPA composites.

This study focuses on the microstructure and magnetic properties of the RPA/IO nanocomposites derived from textile waste. The knowledge gained from this research aims to contribute to the development of sustainable and functional materials, tackling the environmental issues associated with textile waste and promoting resource conservation within the industry.

2. Materials and Methods

2.1. Chemicals

Here, the RPA was prepared according to a patent filed by the State University of Londrina, Brazil (No. BR102013032153A2). Analytical-grade chemicals were used, including ferrous sulfate heptahydrate ($FeSO_4{\cdot}7H_2O$ – Sigma-Aldrich, 99%), ferric chloride hexahydrate ($FeCl_3{\cdot}6H_2O$ – Vetec, 102%), and ammonium hydroxide solution (NH_4OH – Sigma-Aldrich, 30-33%). All chemicals were used as received without further treatment. Solutions were prepared using ultrapure water with a resistivity exceeding 18.00 MΩ·cm, obtained from a water purification system (Elga model USF CE).

2.2. Synthesis of IO Nanoparticles

IO nanoparticles were synthesized by co-precipitation method utilizing salts of Fe^{2+} ($FeSO_4.7H_2O$) and Fe^{3+} ($FeCl_3.6H_2O$) ions in ammonia solution [38]. About 2.78 g portion of $FeSO_4.7H_2O$ and 5.4 g of $FeCl_3.6H_2O$ with a molar ratio of 1:2 was dissolved in 100 mL distilled water with final concentration of 0.3 mol L-1 iron ions. The mixed iron solution was maintained under constant mechanical stirring for 10 minutes to ensure thorough mixing of the ions. Next, 75 mL of NH_4OH was slowly added to the solution at 25°C under vigorous stirring until reaching a pH of 10. Then, the solution was heated to 80°C for 30 minutes, followed by filtration and washing with distilled water. Finally, the precipitate was dried under vacuum oven at 60 °C and stored.

Preprints.org (www.preprints.org) | NOT PEER-REVIEWED | Posted: 14 November 2024 doi:10.20944/preprints202411.1029.v1

2.3. Synthesis of RPA/IO Nanocomposites

RPA/IO nanocomposites were synthesized following the same procedure as above, with the addition of RPA alongside the iron salts. After dissolving the iron salts in 100 mL of water, 4 g of RPA was added. The remaining steps, including NH_4OH addition, heating, filtration, washing, and drying, were performed as described for the IO nanoparticle synthesis.

3. Materials Characterization

X-ray diffraction (XRD) patterns were acquired using a Panalytical Xpert PRO MPD diffractometer with CuKα radiation (λ=0.154 nm). A 2θ scanning range of 20° to 70° was employed with a step size of 0.05°s-1. Rietveld refinement analysis [39] was performed on the XRD patterns using the High Score Plus software (version 3.0). The average crystallite size (S) was determined using the well-known Debye–Scherrer formula, as presented in Equation (1) [40,41]:

$S = k\lambda/\beta \cos \theta$ (1),

where S is the average size of the crystallite (nm), k (0.89) is the Scherrer constant, λ is the X-ray wavelength (0.15406 nm), β is the half-peak width of the diffraction peak (in radians), and θ is the Bragg diffraction angle (in degrees). The degree of crystallinity percentage (%DOC) was calculated by applying Equation (2) [42]:

$\%DOC = 100 \times (Ac/AT)$ (2),

where Ac is the area under crystalline peaks and AT is the total area (area of crystalline and amorphous peaks).

Scanning electron microscopy (SEM) was conducted on a JEOL-FEG JSM-7100F electron microscope at 5 kV, utilizing secondary electrons for imaging. Samples were mounted on stubs with double-sided carbon tape and sputter-coated with a 20 nm gold layer (SCD 050, BAL-TEC BALZERS, Liechtenstein).

Transmission electron microscopy (TEM) was performed on a JEOL 2100F microscope equipped with a Thermo SEVEN detector for energy-dispersive X-ray spectroscopy (EDXS) operating at 200 kV. Samples were prepared by dispersing the powder in isopropyl alcohol using ultrasound for 20 minutes. A drop of the suspension was then deposited onto a copper grid with a carbon film, followed by solvent evaporation.

^{57}Fe Mössbauer spectroscopy in transmission mode was performed using a 57Co source embedded in an Rh matrix with constant acceleration. Calibration was done using an α-Fe foil, and measurements were taken at room temperature. Hyperfine parameters were calculated using a Lorentzian line shape and the minimum chi-square method.

Magnetic properties were assessed using a SQUID-VSM spectrometer (Quantum Design MPSM XL) at 5 and 300k, applying a magnetic field ranging from -20 to 20 kOe.

4. Results and Discussion

4.1. Microstructural Properties

Figure. 1 (a-f) presents the XRD patterns, Rietveld refinement and SEM images of these samples under investigation. The peak positions (2θ) and β values were extracted from these XRD patterns to characterize the microstructure (Table 1). As show in Figure 1(a), the diffraction peaks at the 2θ values of 18.4° (111), 30.3° (220), 35.6° (311), 37.4° (222), 43.3° (400), 54.1° (422), 57.3° (511), and 63.3° (440), correspond to the face-centered cubic structure (belonging to the space group $Fd\bar{3}m$, No. 227) of both Fe_3O_4 and γ-Fe_2O_3 phases, aligning with the Joint Committee on Powder Diffraction Standards (JCPDS) card no. 01-088-0315 for magnetite [43] and card no. 01-076-3168 for maghemite [44], respectively. Similar findings have been reported in the literature [27,45,46]. The peak with the most intense at 2θ = 35.5° (311) in IO sample was chosen to calculate the S value, which is about 10.0 nm and the %DOC was determined in 69.2%. Additionally, the Rietveld refinement method was used to analyze the purity and confirmed the long-range structure of the mixed-phase IO nanostructure (with experimental lattice values of a = 8.384 Å for Fe_3O_4 and a = 8.362 Å for γ-Fe_2O_3) of this sample. The proportions of the Fe_3O_4 and γ-Fe_2O_3 phases were found to be 79.4 wt% and 20.6 wt%, respectively.

Herein, the GOF = 1.52 indicates a good quality of the fit. During synthesis, iron ions (Fe^{2+} and Fe^{3+}) precipitate in an alkaline medium, forming Fe_3O_4, which has an inverse spinel structure belonging to the space group $Fd\bar{3}m$ (No. 227). However, exposure to oxygen in the air oxidizes the Fe^{2+} ions on the surface of magnetite, converting it to γ-Fe_2O_3, which also has a spinel structure but with all iron ions in the Fe^{3+} state.

Figure 1(b) reveals an amorphous halo ranging from 2θ = 18° to 26°, indicative of the amorphous nature of the RPA material. Superimposed on this halo are two distinct crystalline peaks at 20.1° and 23.6°, corresponding to the (200) and (002) planes, respectively. These peaks are characteristic of the α-form crystal structure commonly observed in PA materials [47,48], suggesting the presence of some crystalline regions within the predominantly amorphous RPA structure [9,49]. For the RPA, the calculated S values for the (200) and (002) planes were found to be 3.2 and 2.9 nm, respectively, while the %DOC of RPA was measured at 35.8% (Table 1). These findings are consistent with the literature on various PAs. For example, Qianhui et al. [50] used CaCl2/ethanol/water-based solvents to analyze waste PA and RPA. Both materials showed two crystalline peaks at 20.2° and 23.5°, indicating the α crystal form. The %DOC was 52.0% for waste PA and 35.9% for RPA. Similarly, Colucci et al. [51] studied the effect of mechanical recycling on the microstructure and properties of PA composites reinforced with carbon fibers. They identified the α crystal form in PA with 2θ peaks near 20° and 24°, respectively. The %DOC calculated at 26.2% for PA66 and 24.6% for RPA. These studies suggest that recycling, whether through solvents or mechanical processes, may decrease the crystallinity of PAs. This is likely due to partial degradation or structural changes during recycling.

As shown in Figure 1(e), the SEM micrographs reveals that the RPA sample exhibits an irregular morphology, characterized by a rough surface and several pores in the micrometer range. High porosity surfaces are desired for multifunctional nanocomposites, because it facilitates molecule entry, making it a promising material for adsorbing emerging pollutants due to its porous nature [52,53]. Additionally, RPA's surface of is abundant in oxygen and nitrogen atoms, which enables interactions with positively charged ions, further enhancing its adsorption capabilities [54,55].

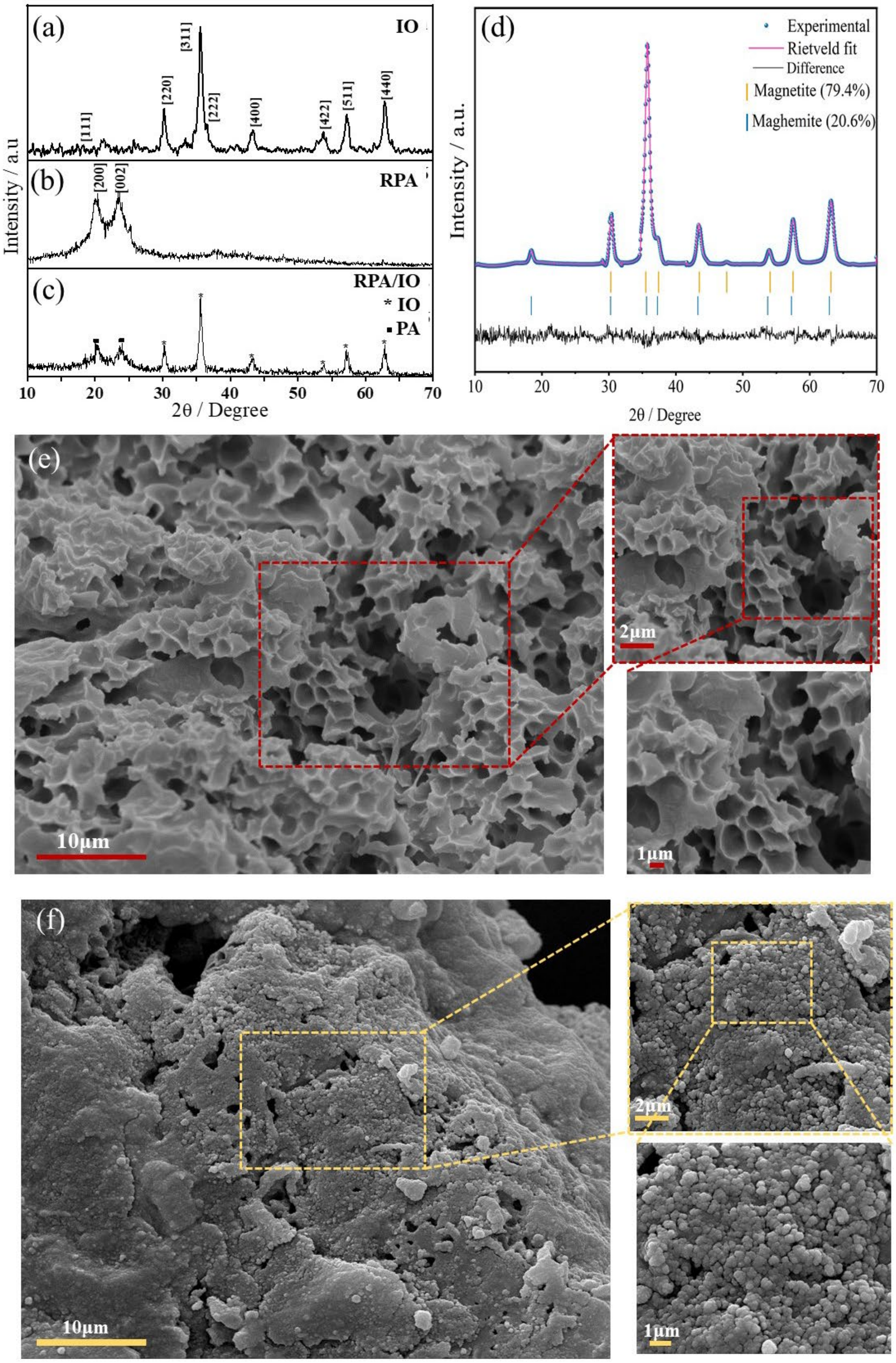

Figure 1. XRD patterns of IO (a), RPA (b), and RPA/IO nanocomposite (c); Rietveld plot for the IO nanostructure (d); SEM micrographs of RPA (e), and RPA/IO nanocomposite (f).

Table 1. Size parameters for the calculation of average crystallite size (S), and the degree of crystallinity percentage (%DOC).

Sample	Planes/ h k l	2θ°	*β	**S / nm	***%DOC
IO	311	35.6	0.8341	10.0	69.2

RPA	200	20.1	2.6408	3.2	35.8
	002	23.6	3.0403	2.9	
RPA / IO	200	20.3	1.9383	4.4	11.5
	002	23.9	1.8330	4.6	

*β is the half-peak width of the diffraction peak. **S is the average crystallite size. ***%DOC is the degree of crystallinity percentage.

Regarding RPA/IO nanocomposites, the XRD patterns revealed the presence of characteristic RPA peaks alongside multiple crystalline peaks attributable to the mixed-phase IO nanostructure (Figure 1c). The Bragg intensities were characterized at 2θ angles of 20.3° (200), 23.9° (002), 30.2° (220), 35.6° (331), 43.4° (400), 54.4° (422), 57.3° (511), and 63.5° (440). A prominent IO crystalline peak was observed at 2θ = 35.6, corresponding to the (311) plane. The impact of incorporating IO into the RPA/IO nanocomposites was analyzed by calculating the S values and %DOC from the peaks at 20.3° and 23.9°, which were found to be 4.4 nm and 4.6 nm, respectively, with a %DOC of 11.5% (Table 1). These results indicated a slight increase in the S value compared to the bare RPA sample. Conversely, the %DOC decreased by approximately 24%, indicating a significant influence of IO on the crystalline structure of the resulting nanocomposite.

Furthermore, SEM micrographs in Figure 1(f) provide insights into the morphology and distribution of the IO with the nanocomposite. These results show that these nanostructures, exhibiting an almost spherical shape, are unevenly dispersed on the RPA surface but instead form aggregates. This creates a unique nanocomposite structure with several potential advantages. First, the porous nature of the RPA surface offers a high surface area for IO nanostructure to adhere to. This enhanced the interaction between the RPA matrix and the IO can lead to stronger interfacial interactions, improving overall stability and mechanical properties of nanocomposite. Second, the uneven dispersion and formation of IO aggregates can create localized regions of concentrated magnetic activity. This could significantly enhance the nanocomposite's performance in applications that rely on magnetic properties, such as magnetic separation, catalysis, or sensors [19,56,57].

Figure 2 depicts the TEM images, particle size distributions, and selected area electron diffraction (SAED) patterns for both IO and the RPA/IO nanocomposite. The spherical morphology of the IO is confirmed by the TEM image (Figure 2a). The SAED pattern confirms the polycrystalline nature of the inverse spinel IO structure (Figure 2c), as indicated by the rings corresponding to the (111), (220), (311), and (400) planes [58]. From the SAED results, the lattice parameter was calculated to be 8.369 Å, which is consistent with Rietveld refinement of the XRD data. Figure 2(b) displays a well-ordered (311) lattice plane is attributed to the principal crystalline peak of the IO phase with an average particle size of about 15.3 ± 0.3 nm. Hence, the agglomerated IO can be observed in Figure 2(d), which is consistent with the SEM results. HRTEM image reveals the crystalline nature of IO (Figure 2e), while SAED and XRD patterns confirms the IO phase (Figure 2f). The bright field TEM images of the RPA/IO nanocomposite, presented in Figure 3g, indicate the nanoparticle nature of the synthesized IO powder, which has an average particle size of approximately 14.1 ± 0.2 nm and an irregular quasi-spherical morphology. Additionally, the EDX mapping indicates that the RPA/IO nanocomposite is rich in Fe and O, with the C content associated with both IO and RPA phases, and no other contaminating elements. Hence, the presence of the IO in nanocomposite suggests that this functional material likely exhibits magnetic properties.

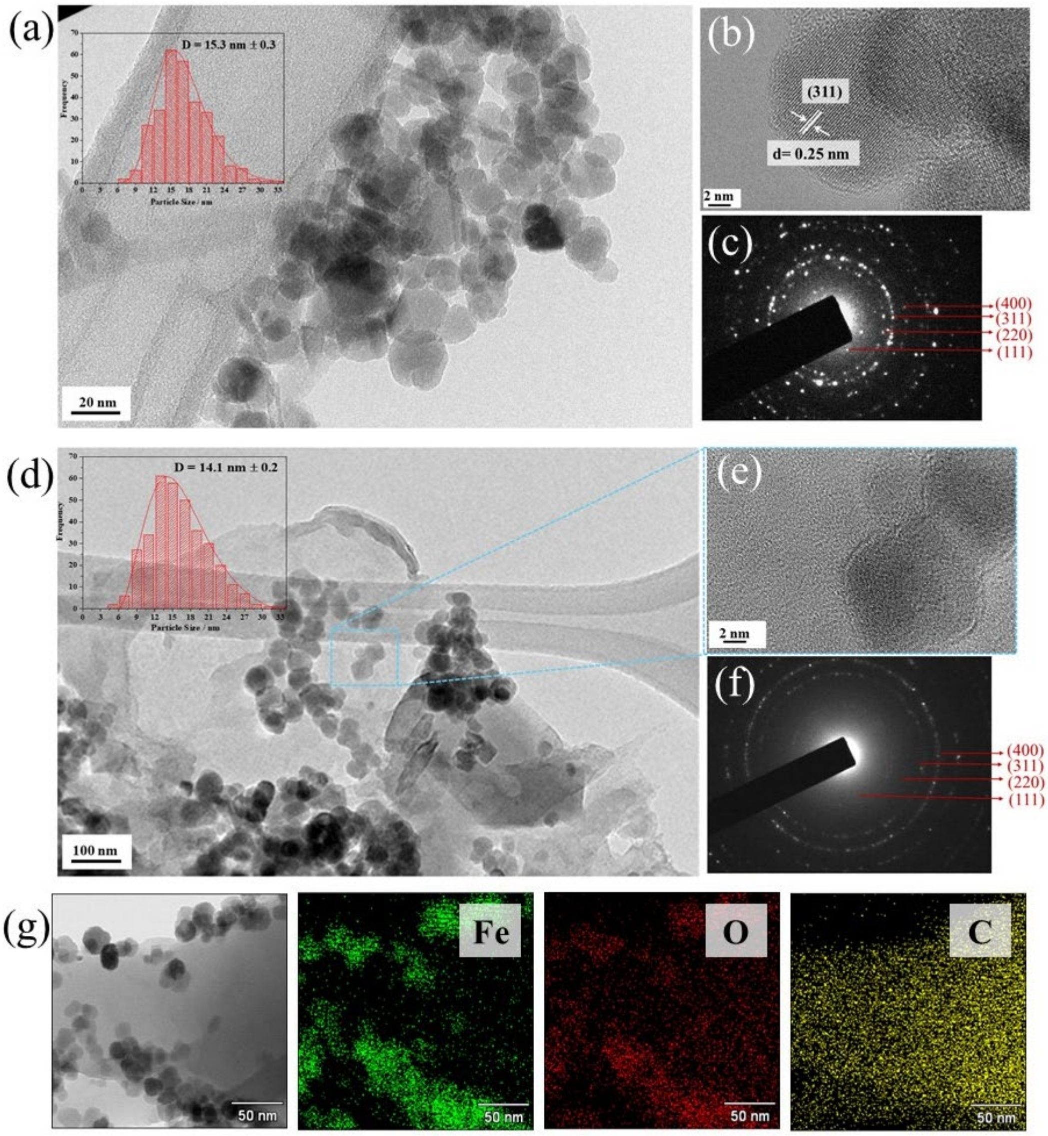

Figure 2. Low-magnification and high-magnification TEM images with SAED patterns of both IO (2a, 2b, and 2c) and RPA/IO nanocomposite (2d, 2e, and 2f). EDX mapping of the RPA/IO nanocomposite showing Fe, O and C elements (g).

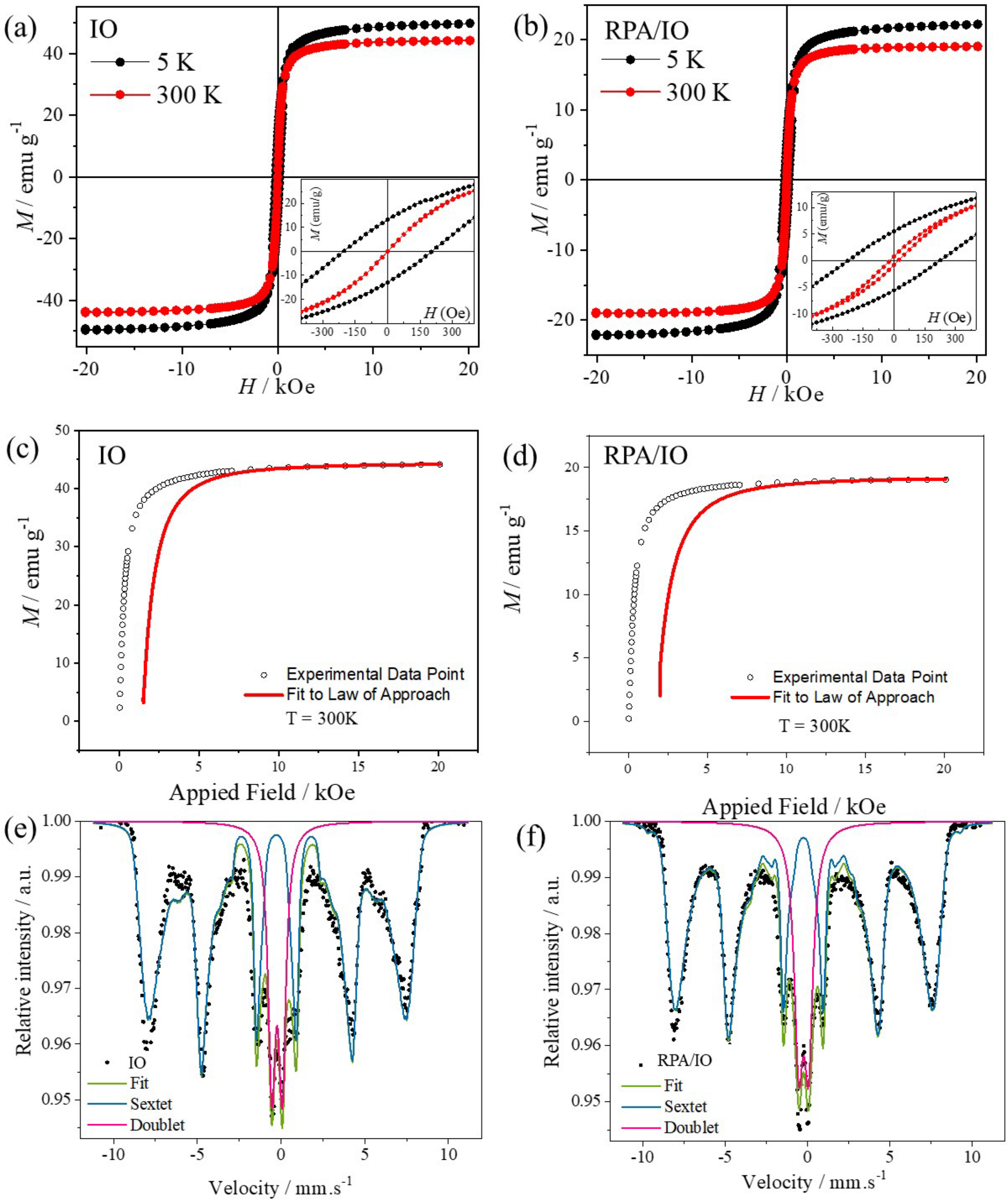

Figure 3. M–H Loops at 5 K and 300 K (a and b), and the law of approach to saturation for IO (c) and RPA/IO nanocomposites (d). Mössbauer spectra of IO (e), and RPA/IO nanocomposite (f) at room temperature.

4.2. Magnetic Properties

To study the magnetic behavior of the IO and RPA/IO nanocomposites, magnetization measurements as a function of the magnetic field were performed. In the VSM measurements, the saturation magnetization (Ms), remnant magnetization (Mr), and coercivity (Hc) were extracted from the hysteresis curves at 5 K and 300 K (see Table 2 and Figure 3). The mixed-phase IO nanostructure exhibited a MS of 50.0 emu g^{-1} at 5K, lower than that of bulk magnetite [45,59,60], likely due to the presence of both Fe_3O_4 and γ- Fe_2O_3 phases as identified by Rietveld refinement of XRD data. This presence of multiple phases could lead to a decrease in the overall Ms value observed for the IO, as the magnetic properties of the mixed phases can result in a lower effective magnetization compared to pure bulk Fe_3O_4 [48,61,62]. At 300 K, the Ms, Mr, and Hc values were calculated as follows: Ms = 44.1 emu g^{-1}, Mr = 0.7 emu g^{-1}, and Hc = 2.5×10^{-4} kOe, respectively. Hu et al. [60] suggest that the magnetic properties of these materials are significantly influenced by their crystallinity and the method used for their synthesis. As observed in Figure 3(a), the curve for the IO at 300 K does not show any hysteresis loop and exhibits low Hc (2.5×10^{-4} KOe) and Mr (0.7 emu g^{-1}) values. At 300 K, the absence of a hysteresis loop and significantly reduced Mr and Hc suggest a transition to superparamagnetic behavior [63]. Conversely, the presence of a hysteresis loop at 5 K suggests ferrimagnetic behavior, as the reduced thermal energy allows the magnetic moments to align and remain aligned. These findings are consistent with previous studies in the literature [63–65]. Chirita et al. [64] synthesized magnetite nanoparticles and studied the magnetic properties, particularly the effect of temperature. They recorded magnetization curves within the 5–300 K, observing a decreased in hysteresis loop as the temperature increased. Above 150 K, the cubic inverse spinel phase exhibited a nearly hysteresis-free magnetization cycle. Based on these findings, they concluded that the IO demonstrate a superparamagnetic-like behavior.

For RPA/IO nanocomposites, the Ms values at 5 K and 300 K were measured at 22.2 and 19.1 emu g^{-1}, respectively, which are 50% lower compared to those of the pure IO. Additionally, the RPA/IO nanocomposites exhibit hysteresis loops at both temperatures, with the loops being less pronounced at 300 K. This reduction in magnetic properties relative to pure IO is likely due to the interaction between the polymer matrix and the IO. The presence of RPA may be disrupting the Fe-O-Fe interactions by altering the local structure or surrounding environment of the IO nanostructure. We hypothesize that RPA could interfere with the formation or stability of the oxide layer on the IO, potentially modifying the interactions between iron atoms and, consequently, impacting magnetization.

As shown in Table 2, the magnetic moment ratio (Mr/Ms) was found to be below 0.3 for all samples. At the elevated temperature of 300 K, these Mr/Ms ratios further decreased to 0.02 for IO and 0.04 for RPA/IO nanocomposite. This reduction is likely associated with the material's magnetic anisotropy [66], which can diminish at higher temperatures, leading to a more disordered state [67]. This disorder results in a lower Mr relative to the Ms. Additionally, the distribution and density of IO on the RPA surface significantly influence the magnetization behavior of the nanocomposites [66]. SEM and TEM analysis confirmed the aggregation of IO nanostructure, which can influence magnetic anisotropy and exchange interactions, thereby contributing to the observed variations in Ms values in RPA/IO nanocomposites.

In our study, the magnetic IO and the RPA/IO nanocomposite exhibit superparamagnetic behavior at 300 K, a characteristic of systems with single-domain particles [68]. In such systems, the absence of domain walls means that the magnetization reversal mechanism is primarily driven by magnetic anisotropy [69]. This anisotropy arises from a combination of magnetocrystalline, shape, strain, and surface anisotropies, with its magnitude represented by the magnetic anisotropy constant (K), which quantifies anisotropy energy per unit volume. For spherical magnetic nanoparticles, the dominant contribution typically comes from magnetocrystalline anisotropy, expressed by the magnetocrystalline anisotropy constant (K_1) [70,71]. As the SEM micrographs and TEM images illustrated that the IO in our samples are almost spherical, we can reasonably approximate K as K_1 in this study, making the magnetocrystalline anisotropy the primary focus for understanding the anisotropic properties of these nanoparticles.

To investigate magnetic anisotropy, the initial magnetization curves of the samples were fitted using the law of approach to saturation (LAS), which facilitates the estimation of the constant, K_1. This approach was utilized to analyze magnetic behavior in the saturation region, illustrating the relationship between magnetization and the applied magnetic field when H≫Hc. The magnetization near saturation can be expressed as follows [72]:

$M = Ms\ [1 - b/H^2] + kH$, (3)

The term b/H^2 represents the rotation of magnetization against the magnetocrystalline anisotropy energy, where $b = 8/105 \times \frac{K_1^2}{\mu_0^2 M_S^2}$ (8/105 is a coefficient related to cubic anisotropy of random polycrystalline samples, K_1 is the cubic anisotropy constant, MS is the saturation magnetization, and

μ_0 is the permeability of free space). H is the applied magnetic field, and kH, referred to as the forced magnetization, behaves similarly to a paramagnetic component, resulting from a linear increase in spontaneous magnetization with the applied magnetic field. Forced magnetization becomes significant under elevated temperatures and very high magnetic fields, necessitating its inclusion in such analyses. However, for the purpose of estimating K_1 value in this study, the term kH was omitted from equation (3). The observed magnetization data for applied magnetic field above 2 kOe at 300 K were fitted using equation (3). The values of Ms and b were then used to estimate the K_1 constant, as shown in Equation (4):

$$K_1 = \mu_0 M_s \sqrt{105b/8} \quad (4),$$

Figure 3c and 3d show the typical LAS fitting curves at 300 K for the IO and RPA/IO nanocomposites, respectively. Table 2 presents the K_1 values of the samples at 300 and 5 K. The K_1 values for the IO and RPA/ IO nanocomposite was estimated to be 4.77×10^5 and 3.53×10^5 at 5 K, respectively, whereas at 300 K, the values were 2.90×10^5 and 1.26×10^5, respectively. Notably, in both cases, the K_1 constant increased as the temperature decreased. According to Paswan et al. [70], magnetic anisotropy in spinel ferrite is caused by spin-orbit interactions and unquenched orbital magnetic moments. At 5 K, the higher K_1 values suggest restricted moment orientations owing to stronger interactions and reduced thermal energy, resulting in stable magnetization. In contrast, the lower K_1 values at 300 K indicate weaker spin-orbit interactions and suppressed orbital magnetic moments. In the superparamagnetic state, particles easily switch magnetization directions, consistent with the lower anisotropy constant observed at 300 K. Therefore, the relationship between K_1, temperature, and magnetic behavior illustrates the transition from a stable ferrimagnetic state at low temperatures to a dynamic superparamagnetic state at higher temperatures.

In the study by Mamiya et al. [73], the magnetic anisotropy constant K_1 ranged from 1.0×10^5 – 2.0×10^5 erg cm^{-3}, values corresponding to pure magnetite nanoparticles. In contrast, our IO sample consisted of both magnetite and maghemite phases, potentially altering the K_1 value owing to differences in crystal structure and cation distribution. Magnetic anisotropy in magnetite results from a combination of factors, including magnetocrystalline anisotropy, shape anisotropy, surface anisotropy, and mechanical stress [73]. Specifically, magnetocrystalline anisotropy is influenced by strong super-exchange interactions between tetrahedral and octahedral sites. The presence of maghemite may affect these interactions, leading to variations in the magnetic anisotropy constant compared to pure magnetite nanoparticles. Moreover, for nanoparticles of volume V, the magnetic anisotropy constant can be related to the blocking temperature (TB) by the following equation (5) [74]:

T_B = KV/25KB, (5),

where K is the magnetic anisotropy constant; V is the volume of the IO; and KB is the Boltzmann constant. This equation demonstrates that the blocking temperature is directly proportional to the magnetic anisotropy constant K_1 and the volume V of the nanoparticle. This blocking temperature reflects the point at which thermal energy overcomes the energy barrier KV, allowing magnetization to fluctuate. Below TB, magnetization remains “blocked” in a stable direction, while above this temperature, the system transitions to a superparamagnetic state, where magnetization can easily reorient due to thermal fluctuations.

To determine T_B for the samples, K_1 at 300 K was used to investigate temperature-dependent magnetic characteristics (see Table 2). The volume of the nanoparticles was calculated from the diameter obtained through TEM analysis (Figure 2a and 2d). The TB for the IO and RPA/IO nanocomposites was found to be 149 and 147 erg cm^{-3}, respectively. At TB, the IO exhibits ferrimagnetism in the blocked state, whereas above this temperature, it transitions to superparamagnetic behavior. The T_B can vary with particle size, synthesis methods, and interactions [75]. For instance, spherical magnetic nanoparticles with a size of approximately 5.7 nm exhibited a T_B of approximately 28 K under an applied field of 100 Oe [76]. In another study, magnetite nanoparticles with a mean size of 20 nm embedded in polyvinyl alcohol exhibited a T_B of approximately 300 K [77]. Under more specific conditions, including the field and particle size, similar blocking temperatures between 100-200 K have been reported for nanoparticles in the range of 11–18 nm [78,79]. Understanding the temperature dependence of superparamagnetic behavior is crucial for applications requiring particle stability across a range of temperatures.

Table 2. The measured magnetic parameters of IO and RPA/IO nanocomposite at 5 K and 300 K.

Sample	Temperature / K	Ms/emu g^{-1}	Mr/emu g^{-1}	Mr/Ms	Hc / KOe	K$_1$/erg cm^{-3}
IO	5	50.0	13.2	0.26	0.2	4.77×10^5
	300	44.1	0.7	0.02	2.5×10^{-4}	2.90×10^5
RPA/IO	5	22.2	5.5	0.25	0.2	3.53×10^5
	300	19.1	0.8	0.04	0.02	1.26×10^5

Mössbauer spectroscopy was used to quantitatively determine the oxidation states of Fe species and provide insights into the contributions of Fe ions at tetrahedral (FeA) and octahedral ($\mathrm{Fe_B}$) sites in a sample [29,80]. The resulting ^{57}Fe Mössbauer spectra are shown in Figure 3e and 3f, and Table 3 lists the hyperfine parameters obtained. Mössbauer spectrum of IO nanostructure was fitted by considering a magnetic hyperfine field distribution for the FeA–sites and a doublet for the $\mathrm{Fe_B}$–sites within the crystalline structure of the IO. The hyperfine magnetic field distribution for the $\mathrm{Fe_A}$–sites showed an isomer shift (δ) of 0.36 mm s^{-1}, a hyperfine field (Bhf) of 44.7 T, and an intensity of 81.3%, which is characteristic of Fe^{+3} in the tetrahedral environment of magnetite [81]. The doublet component showed a δ of 0.35 mm s^{-1} and an intensity of 18.7%, characteristic of high-spin Fe^{3+}, attributed to the γ- Fe_2O_3 phase in the IO sample.

As depicted in Figure 3e, Fe^{3+} ions occupy the $\mathrm{Fe_A}$ sites, with oxygen coordination. Fe^{2+} and Fe^{3+} ions are distributed equally between the $\mathrm{Fe_A}$ and $\mathrm{Fe_B}$ sites, resulting in an overall occupancy of 1/8 at $\mathrm{Fe_A}$ and 1/2 for $\mathrm{Fe_B}$ sites [82]. The γ-Fe_2O_3 phase crystallizes in a similar cubic spinel structure but with a tetragonal supercell and a lattice constant of 8.33 Å [83]. Unlike magnetite, maghemite contains only Fe^{3+} ions, which are randomly distributed across 16 $\mathrm{Fe_B}$ and 8 $\mathrm{Fe_A}$ interstitial sites. These results align with those reported in previous studies [84–86].

The conversion of Fe^{2+} ions to Fe^{3+} ions during oxidation, leading to iron vacancies to maintain charge balance. This transformation can occur under various conditions, such as natural weathering or hydrothermal treatments, altering the crystal structure [81,82]. The presence of iron vacancies on maghemite surfaces influences its reducibility, oxidation potential, and overall properties. Mössbauer spectra of the IO nanostructure can be successfully interpreted as a mixture of magnetite and maghemite, rather than as nonstoichiometric magnetite. This interpretation aligns with previous reports [27,61,83].

For the RPA/IO nanocomposite, the spectra were fitted using a model that accounted for the magnetic hyperfine field distribution at $\mathrm{Fe_A}$ sites and a doublet at $\mathrm{Fe_B}$ sites. The δ value and Bhf for the first component were 0.34 mm s^{-1} and 45.8 T, respectively. The second component had a δ value of 0.35 mm s^{-1}. The intensities of the first component and second components were 78.8% and 21.1%, respectively. Mössbauer spectroscopy results revealed that the incorporation of RPA did not significantly change the crystalline structure of IO in the nanocomposite. This finding is consistent with the XRD patterns shown in Figure 1c.

Table 3. Mössbauer hyperfine parameters for studied samples. δ: isomer shift; ΔE_Q: quadrupole shift; Bhf: hyperfine magnetic field; Γ: resonance linewidth; Area: relative area.

Sample	^{57}Fe Site	δ / mm s^{-1}	ΔE_Q / mm s^{-1}	B_{hf} /T	Γ / mm s^{-1}	Area /%
IO	Distribution	0.36	0.05	44.7	-	81.3
	Doublet	0.35	0.62	-	0.52	18.7

RPA	-	-	-	-	-	-
RPA/IO	Distribution	0.34	0.04	45.8	-	78.8
	Doublet	0.35	0.60	-	0.66	21.2

5. Conclusions

In conclusion, this study successfully demonstrated the fabrication of a novel RPA/IO nanocomposite using recycled textile PA. The comprehensive characterization through XRD, SEM, TEM, VSM, and Mössbauer spectroscopy confirmed the successful synthesis, microstructure and magnetic properties of this nanocomposite. XRD analysis revealed a semi-crystalline structure with an S value of 10.0 nm and a degree of crystallinity of 11.5%, while SEM and TEM showed a nanometric scale and porous morphology, with IO well-dispersed on the nanocomposite's surface. The observed average particle size of 14 nm aligns with expectations for such materials. Magnetic measurements demonstrated temperature-dependent behavior, with Mössbauer spectroscopy indicating the presence of a maghemite phase likely due to surface oxidation.

This study highlights the potential of recycled PA as a valuable resource for developing cost-effective and functional nanocomposites, contributing to both material science and sustainable efforts. The simple preparation method and the promising properties of the RPA/IO nanocomposite suggest its suitability for a range of applications. Future research will focus on scaling up the production process and evaluation the nanocomposite's performance in specific applications, such as those requiring magnetic properties or enhanced mechanical strength.

Author Contributions: L.G.D.S., D.F.V., E.D., D. D. A. B. Conceptualization, conceived, writing—review and editing, B. L. S. V., F. D. A. L. P., C.M.M.R. validation, methodology and investigation All authors discussed the results and contributed to the final manuscript. All authors have read and agreed to the published version of the manuscript.

Funding: This research was funded by CNPq project 172349/2023-0

Institutional Review Board Statement: Not applicable.

Informed Consent Statement: Not applicable.
Data Availability Statement: Data are contained within the article.

Acknowledgments: The authors gratefully acknowledge the National Council for Scientific and Technological Development (CNPq, Process no. 172349/2023-0) for the postdoctoral fellowship, and CAPES, CNPq, and Fundação Araucária for the financial support through scholarships. The authors also extend they're thanks to the Gleb Wataghin Institute of Physics (IFGW) at the University of Campinas (UNICAMP), Campinas, SP, Brazil, for providing facilities for magnetic measurements, the Group of Special Materials at the Physics Department of the State University of Maringá (UEM), Maringá, PR, Brazil, for conducting the Mössbauer analysis, and the Department of Chemical and Materials Engineering at PUC-Rio, Rio de Janeiro, Brazil, for assistance with microscopic measurements.

Conflicts of Interest: The authors declare no conflicts of interest.

References

1. Koszewska, M. Circular Economy - Challenges for the Textile and Clothing Industry. Autex Res. J. 2018, 18 (4), 337–347. https://doi.org/10.1515/AUT-2018-0023.
2. Roy Choudhury, A. K. Environmental Impacts of the Textile Industry and Its Assessment Through Life Cycle Assessment. 2014, 1–39. https://doi.org/10.1007/978-981-287-110-7_1.
3. Juanga-Labayen, J. P.; Labayen, I. V.; Yuan, Q. A Review on Textile Recycling Practices and Challenges. Text. 2022, Vol. 2, Pages 174-188 2022, 2 (1), 174–188. https://doi.org/10.3390/TEXTILES2010010.
4. Wang, Y. Fiber and Textile Waste Utilization. Waste and Biomass Valorization 2010, 1 (1), 135–143. https://doi.org/10.1007/S12649-009-9005-Y.
5. Tang, K. H. D. State of the Art in Textile Waste Management: A Review. Text. 2023, Vol. 3, Pages 454-467 2023, 3 (4), 454–467. https://doi.org/10.3390/TEXTILES3040027.

6. Patwary, S. Clothing and Textile Sustainability: Current State of Environmental Challenges and the Ways Forward. Text. Leather Rev. 2020, 3 (3), 158–173. https://doi.org/10.31881/TLR.2020.16.
7. Markovičová, L.; Zatkalíková, V.; Kojnoková, T. Environmental Impact on the Life of a Polymeric Composite with Polyamide Matrix and Glass Fibres. IOP Conf. Ser. Mater. Sci. Eng. 2021, 1178 (1), 012043. https://doi.org/10.1088/1757-899X/1178/1/012043.
8. Hirschberg, V.; Rodrigue, D. Recycling of Polyamides: Processes and Conditions. J. Polym. Sci. 2023, 61 (17), 1937–1958. https://doi.org/10.1002/POL.20230154.
9. Al-Shawabkeh, A. F. Optoelectronic Investigation and Spectroscopic Characteristics of Polyamide-66 Polymer. E-Polymers 2022, 22 (1), 858–869. https://doi.org/10.1515/EPOLY-2022-0078.
10. Hashemi Sanatgar, R.; Campagne, C.; Nierstrasz, V. Investigation of the Adhesion Properties of Direct 3D Printing of Polymers and Nanocomposites on Textiles: Effect of FDM Printing Process Parameters. Appl. Surf. Sci. 2017, 403, 551–563. https://doi.org/10.1016/J.APSUSC.2017.01.112.
11. Baeg, K.-J.; Lee, J.; Baeg, -J K; Lee, J. Flexible Electronic Systems on Plastic Substrates and Textiles for Smart Wearable Technologies. Adv. Mater. Technol. 2020, 5 (7), 2000071. https://doi.org/10.1002/ADMT.202000071.
12. Koronis, G.; Silva, A.; Fontul, M. Green Composites: A Review of Adequate Materials for Automotive Applications. Compos. Part B Eng. 2013, 44 (1), 120–127. https://doi.org/10.1016/J.COMPOSITESB.2012.07.004.
13. Mahalik, N. P.; Nambiar, A. N. Trends in Food Packaging and Manufacturing Systems and Technology. Trends Food Sci. Technol. 2010, 21 (3), 117–128. https://doi.org/10.1016/J.TIFS.2009.12.006.
14. Singh, R.; Kumar, R.; Ranjan, N.; Penna, R.; Fraternali, F. On the Recyclability of Polyamide for Sustainable Composite Structures in Civil Engineering. Compos. Struct. 2018, 184, 704–713. https://doi.org/10.1016/J.COMPSTRUCT.2017.10.036.
15. Yao, W. H. The Preparation of Modified Polyamide Clay Nanocomposite/Recycled Maleic Anhydride Polyamide 6 and Blending with Low Density Polyethylene for Film Blowing Application. Polym. Polym. Compos. 2021, 29 (9_suppl), S631–S643. https://doi.org/10.1177/09673911211015000.
16. Medeiros, D. G.; Jardim, P. M.; De Tatagiba, M. K. V.; D'Almeida, J. R. M. Composites of Recycled Nylon 11 and Titanium Based Nanofillers. Polym. Test. 2015, 42, 108–114. https://doi.org/10.1016/J.POLYMERTESTING.2015.01.006.
17. Benaducci, D.; de Oliveira, V.; Yin Tze, W. T.; Hafez, I.; Branciforti, M. C. Nanocomposites of Recycled and of Virgin Polyamide 6.6 with Cellulose Nanofibers. Hybrid Adv. 2024, 6, 100261. https://doi.org/10.1016/J.HYBADV.2024.100261.
18. Korkees, F.; Aldrees, A.; Barsoum, I.; Alshammari, D. Functionalised Graphene Effect on the Mechanical and Thermal Properties of Recycled PA6/PA6,6 Blends. J. Compos. Mater. 2021, 55 (16), 2211–2224. https://doi.org/10.1177/0021998320987897.
19. Bassyouni, D.; Mohamed, M.; El-Ashtoukhy, E. S.; El-Latif, M. A.; Zaatout, A.; Hamad, H. Fabrication and Characterization of Electrospun Fe3O4/o-MWCNTs/Polyamide 6 Hybrid Nanofibrous Membrane Composite as an Efficient and Recoverable Adsorbent for Removal of Pb (II). Microchem. J. 2019, 149, 103998. https://doi.org/10.1016/J.MICROC.2019.103998.
20. Liang, Y.; Xia, X.; Luo, Y.; Jia, Z. Synthesis and Performances of Fe2O3/PA-6 Nanocomposite Fiber. Mater. Lett. 2007, 61 (14–15), 3269–3272. https://doi.org/10.1016/J.MATLET.2006.11.051.
21. Cornell, Rochelle M., and U. S. The Iron Oxides: Structure, Properties, Reactions, Occurrences, and Uses.; Weinheim: Wiley-vch, Ed.; De Gruyter, 2003; Vol. 664. https://doi.org/10.1515/CORRREV.1997.15.3-4.533.
22. Gutierrez, F. V.; De Falco, A.; Yokoyama, E.; Mendoza, L. A. F.; Luz-Lima, C.; Perez, G.; Loreto, R. P.; Pottker, W. E.; La Porta, F. A.; Solorzano, G.; Arsalani, S.; Baffa, O.; Araujo, J. F. D. F. Magnetic Characterization by Scanning Microscopy of Functionalized Iron Oxide Nanoparticles. Nanomater. 2021, Vol. 11, Page 2197 2021, 11 (9), 2197. https://doi.org/10.3390/NANO11092197.
23. Mohapatra, M.; Anand, S. Synthesis and Applications of Nano-Structured Iron Oxides/Hydroxides – a Review. Int. J. Eng. Sci. Technol. 2010, 2 (8), 127–146. https://doi.org/10.4314/IJEST.V2I8.63846.
24. Hamed, M. H.; Mueller, D. N.; Müller, M. Thermal Phase Design of Ultrathin Magnetic Iron Oxide Films: From Fe3O4 to γ-Fe2O3 and FeO. J. Mater. Chem. C 2020, 8 (4), 1335–1343. https://doi.org/10.1039/C9TC05921K.
25. Li, Z.; Chanéac, C.; Berger, G.; Delaunay, S.; Graff, A.; Lefèvre, G. Mechanism and Kinetics of Magnetite Oxidation under Hydrothermal Conditions. RSC Adv. 2019, 9 (58), 33633–33642. https://doi.org/10.1039/C9RA03234G.
26. Winsett, J.; Moilanen, A.; Paudel, K.; Kamali, S.; Ding, K.; Cribb, W.; Seifu, D.; Neupane, S. Quantitative Determination of Magnetite and Maghemite in Iron Oxide Nanoparticles Using Mössbauer Spectroscopy. SN Appl. Sci. 2019, 1 (12), 1–8. https://doi.org/https://doi.org/10.1007/s42452-019-1699-2.
27. Buelvas, D. D. A.; Camargo, L. P.; Valezi, D. F.; Tupan, L. F. S.; Dall'Antonia, L. H.; Rocha, C. M. M.; Lopez, D. A. S.; Urbano, A.; Vicentin, B. L. S. Impact of Varying Magnetite Nanoparticle Concentrations on the

Structural, Electrical, and Magnetic Properties of Polyaniline-Based Magnetic Nanocomposites. Synth. Met. 2024, 117703. https://doi.org/10.1016/J.SYNTHMET.2024.117703.

28. Bragg, W. H. The Structure of Magnetite and the Spinels. Nat. 1915 952386 1915, 95 (2386), 561–561. https://doi.org/10.1038/095561a0.
29. Wareppam, B.; Kuzmann, E.; Garg, V. K.; Singh, L. H. Mössbauer Spectroscopic Investigations on Iron Oxides and Modified Nanostructures: A Review. J. Mater. Res. 2022 384 2022, 38 (4), 937–957. https://doi.org/10.1557/S43578-022-00665-4.
30. Petrychuk, M.; Kovalenko, V.; Pud, A.; Ogurtsov, N.; Gubin, A. Ternary Magnetic Nanocomposites Based on Core–Shell Fe3O4/Polyaniline Nanoparticles Distributed in PVDF Matrix. Phys. status solidi 2010, 207 (2), 442–447. https://doi.org/10.1002/PSSA.200824421.
31. Buelvas, D. D. A.; Camargo, L. P.; Salgado, I. K. I.; Vicentin, B. L. S.; Valezi, D. F.; Dall'Antonia, L. H.; Tarley, C. R. T.; Mauro, E. Di. Study and Optimization of the Adsorption Process of Methylene Blue Dye in Reusable Polyaniline-Magnetite Composites. Synth. Met. 2023, 292, 117232. https://doi.org/10.1016/J.SYNTHMET.2022.117232.
32. Gupta, R.; Pancholi, K.; De Sa, R.; Murray, D.; Huo, D.; Droubi, G.; White, M.; Njuguna, J. Effect of Oleic Acid Coating of Iron Oxide Nanoparticles on Properties of Magnetic Polyamide-6 Nanocomposite. JOM 2019, 71 (9), 3119–3128. https://doi.org/10.1007/S11837-019-03622-5/FIGURES/8.
33. Muhazeli, N. S.; Nordin, N. A.; Mazlan, S. A.; Abdul Aziz, S. A.; Ubaidillah; Nazmi, N. Mini Review: An Insight on the Fabrication Methods of Smart Magnetic Polymer Foam. J. Magn. Magn. Mater. 2021, 534, 168038. https://doi.org/10.1016/J.JMMM.2021.168038.
34. Buelvas, D. D. A.; Camargo, L. P.; Salgado, I. K. I.; Vicentin, B. L. S.; Valezi, D. F.; Dall'Antonia, L. H.; Tarley, C. R. T.; Mauro, E. Di. Study and Optimization of the Adsorption Process of Methylene Blue Dye in Reusable Polyaniline-Magnetite Composites. Synth. Met. 2023, 292, 117232. https://doi.org/10.1016/J.SYNTHMET.2022.117232.
35. Nordin, A. H.; Ahmad, Z.; Husna, S. M. N.; Ilyas, R. A.; Azemi, A. K.; Ismail, N.; Nordin, M. L.; Ngadi, N.; Siti, N. H.; Nabgan, W.; Norfarhana, A. S.; Azami, M. S. M. The State of the Art of Natural Polymer Functionalized Fe3O4 Magnetic Nanoparticle Composites for Drug Delivery Applications: A Review. Gels 2023, Vol. 9, Page 121 2023, 9 (2), 121. https://doi.org/10.3390/GELS9020121.
36. Li, X.; Li, Z.; Shen, J.; Zheng, Z.; Liu, J. Role of a Nanoparticle Network in Polymer Mechanical Reinforcement: Insights from Molecular Dynamics Simulations. Phys. Chem. Chem. Phys. 2021, 23 (38), 21797–21807. https://doi.org/10.1039/D1CP03153H.
37. Li, X.; Huang, B.; Liu, J.; Hu, X.; Zheng, Z. J. Revealing the Reinforcing Effect of a Nanorod Network on a Polymer Matrix through Molecular Dynamics Simulations. Phys. Chem. Chem. Phys. 2023, 25 (28), 18757–18765. https://doi.org/10.1039/D3CP01437A.
38. Wenlei, X.; Ning, M. Immobilized Lipase on Fe3O4 Nanoparticles as Biocatalyst for Biodiesel Production. Energy and Fuels 2009, 23 (3), 1347–1353. https://doi.org/10.1021/EF800648Y.
39. Rietveld, H. M. Line Profiles of Neutron Powder-Diffraction Peaks for Structure Refinement. urn:issn:0365-110X 1967, 22 (1), 151–152. https://doi.org/10.1107/S0365110X67000234.
40. A., G. X-Ray Diffraction in Crystals. Imperfect Crystals, Amorph. Bodies. Dorer 1963.
41. Stern, P.; Polymer, E. S.-; 1968, undefined. On the Structure of Polypropylene Fibres. Elsevier.
42. Buelvas, D. D. A.; Vicentin, B. L. S.; Urbano, A.; Besegato, J. F.; Hoeppner, M. G.; Galvão, T. D.; Parreira, P. S.; Di Mauro, E. Crystalline Properties and Morphology of Bulk-Fill Dental Resin Composites as Function of Light-Cure Protocol and Composition. Polym. Bull. 2023, 80 (3), 2349–2366. https://doi.org/10.1007/S00289-022-04163-9.
43. Sasaki, S. Radial Distribution of Electron Density in Magnetite, Fe3O4. urn:issn:0108-7681 1997, 53 (5), 762–766. https://doi.org/10.1107/S0108768197007842.
44. Jørgensen, J. E.; Mosegaard, L.; Thomsen, L. E.; Jensen, T. R.; Hanson, J. C. Formation of γ-Fe2O3 Nanoparticles and Vacancy Ordering: An in Situ X-Ray Powder Diffraction Study. J. Solid State Chem. 2007, 180 (1), 180–185. https://doi.org/10.1016/J.JSSC.2006.09.033.
45. Rebodos, R. L.; Vikesland, P. J. Effects of Oxidation on the Magnetization of Nanoparticulate Magnetite. Langmuir 2010, 26 (22), 16745–16753. https://doi.org/https://doi.org/10.1021/la102461z.
46. Rebodos, R. L.; Vikesland, P. J. Effects of Oxidation on the Magnetization of Nanoparticulate Magnetite. Langmuir 2010, 26 (22), 16745–16753. https://doi.org/https://doi.org/10.1021/la102461z.
47. Xia, H.; Zhao, X.; Yang, G. Double in Situ Synthesis of Fe3O4/Polyamide 6 Magnetic Nanocomposite. Mater. Lett. 2013, 98, 90–93. https://doi.org/10.1016/J.MATLET.2013.01.051.
48. Zhang, R.; Zhang, B.; Dou, W.; Wu, Y.; Luo, L. Preparation of Nano- Fe3O4/Nylon Composite Fabric with Magnetic Properties by Post Finishing Method. Fibers Polym. 2019, 20 (7), 1396–1403. https://doi.org/10.1007/S12221-019-1242-5.
49. Ranganathan, P.; Mutharani, B.; Tseng, C.-H.; Tsai, P.-S. The Isothermal and Nonisothermal Crystallization Kinetics and Morphology of Solvent-Precipitated Nylon 66. Polym. 2022, Vol. 14, Page 442 2022, 14 (3), 442. https://doi.org/10.3390/POLYM14030442.

50. Qianhui, X.; Hongmei, H.; Ruishu, Z.; Lina, S.; Jianyong, Y.; Xueli, W. A Non-Destructive, Environment-Friendly Method for Separating and Recycling Polyamide 6 from Waste and Scrap Polyamide 6 Blended Textiles. Text. Res. J. 2023, 93 (13–14), 3327–3340. https://doi.org/10.1177/00405175221148260.
51. Colucci, G.; Ostrovskaya, O.; Frache, A.; Martorana, B.; Badini, C. The Effect of Mechanical Recycling on the Microstructure and Properties of PA66 Composites Reinforced with Carbon Fibers. J. Appl. Polym. Sci. 2015, 132 (29). https://doi.org/10.1002/APP.42275.
52. Morales-Luckie, R. A.; Sánchez-Mendieta, V.; Olea-Mejia, O.; Vilchis-Nestor, A. R.; López-Téllez, G.; Varela-Guerrero, V.; Huerta, L.; Arenas-Alatorre, J. Facile Solventless Synthesis of a Nylon-6,6/Silver Nanoparticles Composite and Its XPS Study. Int. J. Polym. Sci. 2013, 2013 (1), 235850. https://doi.org/10.1155/2013/235850.
53. Sadeghi-Kiakhani, M.; Safapour, S.; Mirnezhad, S. Thermodynamic and Kinetic Studies of the Adsorption Behaviour of the Natural Dye Cochineal on Polyamide 66. Color. Technol. 2018, 134 (4), 308–314. https://doi.org/10.1111/COTE.12342.
54. Cheval, N.; Gindy, N.; Flowkes, C.; Fahmi, A. Polyamide 66 Microspheres Metallised with in Situ Synthesised Gold Nanoparticles for a Catalytic Application. Nanoscale Res. Lett. 2012, 7 (1), 1–9. https://doi.org/10.1186/1556-276X-7-182.
55. Zakaria, Z.; Izzah, Z.; Tarmizi, A.; Jawaid, M.; Hassan, A. Effect of Degree of Deacetylation of Chitosan on Thermal Stability and Compatibility of Chitosan-Polyamide Blend. https://doi.org/10.15376/biores.7.4.5568-5580.
56. Abdel-Rahman, M. A.; El-Said, W. A.; Sayed, E. M.; Abdel-Wahab, A. M. A. Synthesis, Characterization of Some Conductive Aromatic Polyamides/ Fe3O4 NPs/ITO, and Their Utilization for Methotrexate Sensing. Surfaces 2023, 6 (1), 83–96. https://doi.org/10.3390/SURFACES6010007/S1.
57. Yu, D.; Ni, H.; Wang, L.; Wu, M.; Yang, X. Nanoscale-Confined Precursor of CuFe2O4 Mediated by Hyperbranched Polyamide as an Unusual Heterogeneous Fenton Catalyst for Efficient Dye Degradation. J. Clean. Prod. 2018, 186, 146–154. https://doi.org/10.1016/J.JCLEPRO.2018.03.134.
58. Mohan, A.; Singhal, R.; Ramanan, S. R. A Study on the Effect of the Collector Properties on the Fabrication of Magnetic Polystyrene Nanocomposite Fibers Using the Electrospinning Technique. J. Appl. Polym. Sci. 2023, 140 (6), e53461. https://doi.org/10.1002/APP.53461.
59. O'Handley; C., R. Modern Magnetic Materials: Principles and Applications. IEEE Electrical Insulation Magazine. 1999, 13 (4), 768.
60. Hu, P.; Zhang, S.; Wang, H.; Pan, D.; Tian, J.; Tang, Z.; Volinsky, A. A. Heat Treatment Effects on Fe3O4 Nanoparticles Structure and Magnetic Properties Prepared by Carbothermal Reduction. J. Alloys Compd. 2011, 509 (5), 2316–2319. https://doi.org/10.1016/J.JALLCOM.2010.10.211.
61. Schwaminger, S. P.; Bauer, D.; Fraga-García, P.; Wagner, F. E.; Berensmeier, S. Oxidation of Magnetite Nanoparticles: Impact on Surface and Crystal Properties. CrystEngComm 2017, 19 (2), 246–255. https://doi.org/10.1039/C6CE02421A.
62. Faaliyan, K.; Abdoos, H.; Borhani, E.; Afghahi, S. S. S. Magnetite-Silica Nanoparticles with Core-Shell Structure: Single-Step Synthesis, Characterization and Magnetic Behavior. J. Sol-Gel Sci. Technol. 2018, 88 (3), 609–617. https://doi.org/10.1007/S10971-018-4847-Z.
63. Goya, G. F.; Berquó, T. S.; Fonseca, F. C.; Morales, M. P. Static and Dynamic Magnetic Properties of Spherical Magnetite Nanoparticles. J. Appl. Phys. 2003, 94 (5), 3520–3528. https://doi.org/10.1063/1.1599959.
64. Chirita, M.; Bezergheanu, A.; Bazil Cizmas, C.; Ercuta, A. Superparamagnetic-like Micrometric Single Crystalline Magnetite for Biomedical Application Synthesis and Characterization. Magnetochemistry 2023, Vol. 9, Page 5 2022, 9 (1), 5. https://doi.org/10.3390/MAGNETOCHEMISTRY9010005.
65. Zhang, H.; Zhu, G. One-Step Hydrothermal Synthesis of Magnetic Fe3O4 Nanoparticles Immobilized on Polyamide Fabric. Appl. Surf. Sci. 2012, 258 (11), 4952–4959. https://doi.org/10.1016/J.APSUSC.2012.01.127.
66. Gupta, R.; Pancholi, P. V.; Yu, X.; Gupta, L.; Stenning, G. B. G.; Bucknall, D.; Flynn, D.; Pancholi, K. Role of Interface in Optimisation of Polyamide-6/ Fe3O4 Nanocomposite Properties Suitable for Induction Heating. Nano-Structures & Nano-Objects 2023, 34, 100973. https://doi.org/10.1016/J.NANOSO.2023.100973.
67. Yoon, S. Determination of the Temperature Dependence of the Magnetic Anisotropy Constant in Magnetite Nanoparticles. J. Korean Phys. Soc. 2011, 59 (5), 3069–3073. https://doi.org/10.3938/jkps.59.3069.
68. Lee, J. S.; Cha, J. M.; Yoon, H. Y.; Lee, J. K.; Kim, Y. K. Magnetic Multi-Granule Nanoclusters: A Model System That Exhibits Universal Size Effect of Magnetic Coercivity. Sci. Reports 2015 51 2015, 5 (1), 1–7. https://doi.org/10.1038/srep12135.
69. Lima, E.; Brandl, A. L.; Arelaro, A. D.; Goya, G. F. Spin Disorder and Magnetic Anisotropy in Fe3 O4 Nanoparticles. J. Appl. Phys. 2006, 99 (8). https://doi.org/10.1063/1.2191471/292707.
70. Paswan, S. K.; Kumari, S.; Kar, M.; Singh, A.; Pathak, H.; Borah, J. P.; Kumar, L. Optimization of Structure-Property Relationships in Nickel Ferrite Nanoparticles Annealed at Different Temperature. J. Phys. Chem. Solids 2021, 151, 109928. https://doi.org/10.1016/J.JPCS.2020.109928.

71. Rondinone, A. J.; Samia, A. C. S.; Zhang, Z. J. Characterizing the Magnetic Anisotropy Constant of Spinel Cobalt Ferrite Nanoparticles. Appl. Phys. Lett. 2000, 76 (24), 3624–3626. https://doi.org/10.1063/1.126727.
72. Chikazumi, S. Physics of Ferromagnetism; Oxford University Press, Ed.; 1997.
73. Muscas, G.; Peddis, D.; Cobianchi, M.; Lascialfari, A.; Cannas, C.; Musinu, A.; Omelyanchik, A.; Rodionova, V.; Fiorani, D.; Mameli, V. Magnetic Interactions Versus Magnetic Anisotropy in Spinel Ferrite Nanoparticles. IEEE Magn. Lett. 2019, 10. https://doi.org/10.1109/LMAG.2019.2956908.
74. Knobel, M.; Nunes, W. C.; Socolovsky, L. M.; De Biasi, E.; Vargas, J. M.; Denardin, J. C. Superparamagnetism and Other Magnetic Features in Granular Materials: A Review on Ideal and Real Systems. J. Nanosci. Nanotechnol. 2008, 8 (6), 2836–2857. https://doi.org/10.1166/JNN.2008.15348.
75. Rumpf, K.; Granitzer, P.; Morales, P. M.; Poelt, P.; Reissner, M. Variable Blocking Temperature of a Porous Silicon/Fe3O4 Composite Due to Different Interactions of the Magnetic Nanoparticles. Nanoscale Res. Lett. 2012, 7 (1), 1–4. https://doi.org/10.1186/1556-276X-7-445/FIGURES/4.
76. Mercante, L. A.; Melo, W. W. M.; Granada, M.; Troiani, H. E.; MacEdo, W. A. A.; Ardison, J. D.; Vaz, M. G. F.; Novak, M. A. Magnetic Properties of Nanoscale Crystalline Maghemite Obtained by a New Synthetic Route. J. Magn. Magn. Mater. 2012, 324 (19), 3029–3033. https://doi.org/10.1016/J.JMMM.2012.04.049.
77. Gogoi, B.; Das, U. Enhanced Study of Magnetic Properties of Polyvinyl Alcohol-Coated Superparamagnetic Iron Oxide Nanoparticles Below Blocking Temperatures. Powder Metall. Met. Ceram. 2023, 62 (1–2), 41–57. https://doi.org/10.1007/S11106-023-00368-3.
78. Correa, J. R.; Bordallo, E.; Canetti, D.; León, V.; Otero-Díaz, L. C.; Negro, C.; Gómez, A.; Sáez-Puche, R. Structure and Superparamagnetic Behaviour of Magnetite Nanoparticles in Cellulose Beads. Mater. Res. Bull. 2010, 45 (8), 946–953. https://doi.org/10.1016/J.MATERRESBULL.2010.04.012.
79. Zheng, R. K.; Gu, H.; Xu, B.; Zhang, X. X. The Origin of the Non-Monotonic Field Dependence of the Blocking Temperature in Magneticnanoparticles. J. Phys. Condens. Matter 2006, 18 (26), 5905. https://doi.org/10.1088/0953-8984/18/26/010.
80. Vértes, A.; Korecz, L. (László); Burger, K. (Kálmán). Moessbauer Spectroscopy. 1979, 432.
81. Winsett, J.; Moilanen, A.; Paudel, K.; Kamali, S.; Ding, K.; Cribb, W.; Seifu, D.; Neupane, S. Quantitative Determination of Magnetite and Maghemite in Iron Oxide Nanoparticles Using Mössbauer Spectroscopy. SN Appl. Sci. 2019, 1 (12), 1–8. https://doi.org/https://doi.org/10.1007/s42452-019-1699-2.
82. Lavorato, G. C.; de Almeida, A. A.; Vericat, C.; Fonticelli, M. H. Redox Phase Transformations in Magnetite Nanoparticles: Impact on Their Composition, Structure and Biomedical Applications. Nanotechnology 2023, 34 (19), 192001. https://doi.org/10.1088/1361-6528/ACB943.
83. Phan, M. H.; Alonso, J.; Khurshid, H.; Lampen-Kelley, P.; Chandra, S.; Repa, K. S.; Nemati, Z.; Das, R.; Iglesias, Ó.; Srikanth, H. Exchange Bias Effects in Iron Oxide-Based Nanoparticle Systems. Nanomater. 2016, Vol. 6, Page 221 2016, 6 (11), 221. https://doi.org/10.3390/NANO6110221.
84. Moacă, E. A.; Watz, C. G.; Socoliuc, V.; Racoviceanu, R.; Păcurariu, C.; Ianoş, R.; Cîntă-Pînzaru, S.; Tudoran, L. B.; Nekvapil, F.; Iurciuc, S.; Șoica, C.; Dehelean, C. A. Biocompatible Magnetic Colloidal Suspension Used as a Tool for Localized Hyperthermia in Human Breast Adenocarcinoma Cells: Physicochemical Analysis and Complex In Vitro Biological Profile. Nanomater. 2021, Vol. 11, Page 1189 2021, 11 (5), 1189. https://doi.org/10.3390/NANO11051189.
85. Kumar, P.; Kumar, P.; Khanduri, H.; Pathak, S.; Pathak, S.; Singh, A.; Singh, A.; Singh, A.; Basheed, G. A.; Basheed, G. A.; Pant, R. P. Temperature Selectivity for Single Phase Hydrothermal Synthesis of PEG-400 Coated Magnetite Nanoparticles. Dalt. Trans. 2020, 49 (25), 8672–8683. https://doi.org/10.1039/D0DT01318H.
86. Singh, S.; Goswami, N. Structural, Optical, Magnetic and Dielectric Properties of Magnetite (Fe3O4) Nanoparticles Prepared by Exploding Wire Technique. J. Mater. Sci. Mater. Electron. 2021, 32 (22), 26857–26870. https://doi.org/10.1007/S10854-021-07062-3.